

Giant anomalous Hall effect in a ferromagnetic kagome-lattice semimetal

Enke Liu^{1,2*}, Yan Sun^{1*}, Nitesh Kumar¹, Lukas Muechler³, Aili Sun¹, Lin Jiao¹, Shuo-Ying Yang⁴, Defa Liu⁴, Aiji Liang^{5,6}, Qiunan Xu¹, Johannes Kroder¹, Vicky Süß¹, Horst Borrmann¹, Chandra Shekhar¹, Zhaosheng Wang⁷, Chuanying Xi⁷, Wenhong Wang², Walter Schnelle¹, Steffen Wirth¹, Yulin Chen^{5,8}, Sebastian T. B. Goennenwein⁹ and Claudia Felser^{1*}

Magnetic Weyl semimetals with broken time-reversal symmetry are expected to generate strong intrinsic anomalous Hall effects, due to their large Berry curvature. Here, we report a magnetic Weyl semimetal candidate, $\text{Co}_3\text{Sn}_2\text{S}_2$, with a quasi-two-dimensional crystal structure consisting of stacked kagome lattices. This lattice provides an excellent platform for hosting exotic topological quantum states. We observe a negative magnetoresistance that is consistent with the chiral anomaly expected from the presence of Weyl fermions close to the Fermi level. The anomalous Hall conductivity is robust against both increased temperature and charge conductivity, which corroborates the intrinsic Berry-curvature mechanism in momentum space. Owing to the low carrier density in this material and the considerably enhanced Berry curvature from its band structure, the anomalous Hall conductivity and the anomalous Hall angle simultaneously reach $1,130 \Omega^{-1} \text{cm}^{-1}$ and 20%, respectively, an order of magnitude larger than typical magnetic systems. Combining the kagome-lattice structure and the long-range out-of-plane ferromagnetic order of $\text{Co}_3\text{Sn}_2\text{S}_2$, we expect that this material is an excellent candidate for observation of the quantum anomalous Hall state in the two-dimensional limit.

The anomalous Hall effect (AHE) is an important electronic transport phenomenon¹. It can arise because of two qualitatively different microscopic mechanisms: extrinsic processes due to scattering effects, and an intrinsic mechanism connected to the Berry curvature^{1–5}. The large Berry curvature comes from the entangled Bloch electronic bands with spin–orbit coupling when the spatial-inversion or time-reversal symmetry of the material is broken^{6,7}. The quantum AHE in two-dimensional (2D) systems is determined solely by this intrinsic contribution^{8,9}. It manifests itself as a quantized anomalous Hall conductance due to the presence of a bulk gap in combination with dissipationless edge states^{10–13}. A magnetic Weyl semimetal with broken time-reversal symmetry can be interpreted as a stacked heterostructure of such quantum anomalous Hall insulator layers^{14,15}, where the coupling between the layers closes the bulk bandgap at isolated Weyl nodes. At these Weyl nodes, the Berry curvature is enhanced whereas the carrier density vanishes^{2–4,16,17}. This suggests that an intrinsic large anomalous Hall conductivity and a large anomalous Hall angle can be expected in such systems.

To date, a number of promising candidates for magnetic Weyl semimetals have been proposed, including $\text{Y}_2\text{Ir}_2\text{O}_7$ (ref. ¹⁸), HgCr_2Se_4 (ref. ¹⁹) and certain Co_2 -based Heusler compounds^{20–22}. The experimental identifications for this Weyl phase in these systems are also on the way. Indeed, an anomalous Hall angle of approximately 16% was recently observed at low temperatures in the magnetic-field-induced Weyl semimetal GdPtBi (ref. ²³). However, a finite external magnetic field is mandatory to make GdPtBi a Weyl

semimetal. Therefore, the search for intrinsic magnetic Weyl semimetals with Weyl nodes close to the Fermi level is not only an efficient strategy to obtain materials exhibiting both a high anomalous Hall conductivity and large anomalous Hall angle, but also important for a comprehensive understanding of Weyl topological effects on the AHE in real materials.

The kagome lattice has become one of the most fundamental models for exotic topological states in condensed matter physics. In particular, the kagome lattice with out-of-plane magnetization is an excellent platform for investigating the quantum anomalous Hall effect^{24,25}. Thus, it provides an effective guiding principle for realizing magnetic Weyl semimetals via stacking^{14,15}. Although a Dirac dispersion with a finite spin–orbit-coupling-induced gap has recently been observed in a kagome-lattice metal²⁶, the Weyl phase in a magnetic kagome material still remains elusive. Here, we report a time-reversal-symmetry-breaking Weyl semimetal in the magnetic kagome-lattice compound $\text{Co}_3\text{Sn}_2\text{S}_2$ with out-of-plane ferromagnetic order, and demonstrate both a large intrinsic anomalous Hall conductivity ($1,130 \Omega^{-1} \text{cm}^{-1}$) and a giant anomalous Hall angle (20%).

$\text{Co}_3\text{Sn}_2\text{S}_2$, a shandite compound, is known to be a ferromagnet with a Curie temperature (T_C) of 177 K and a magnetic moment of $0.29 \mu_B/\text{Co}$ ^{27–29}. Magnetization measurements have shown that the easy axis of the magnetization lies along the c axis³⁰, while photo-emission measurements and band structure calculations revealed that, below T_C , $\text{Co}_3\text{Sn}_2\text{S}_2$ exhibits Type-IA half-metallic ferromagnetism in which spin-minority states are gapped^{31,32}. Figure 1 summarizes the structural and electronic properties of $\text{Co}_3\text{Sn}_2\text{S}_2$. As shown

¹Max Planck Institute for Chemical Physics of Solids, Dresden, Germany. ²Institute of Physics, Chinese Academy of Sciences, Beijing, China. ³Department of Chemistry, Princeton University, Princeton, NJ, USA. ⁴Max Planck Institute of Microstructure Physics, Halle, Germany. ⁵School of Physical Science and Technology, ShanghaiTech University, Shanghai, China. ⁶Advanced Light Source, Lawrence Berkeley National Laboratory, Berkeley, CA, USA. ⁷High Magnetic Field Laboratory, Chinese Academy of Sciences, Hefei, China. ⁸Clarendon Laboratory, Department of Physics, University of Oxford, Oxford, UK. ⁹Institut für Festkörper- und Material Physik, Technische Universität Dresden, Dresden, Germany. *e-mail: ekliu@iphy.ac.cn; yan.sun@cpfs.mpg.de; Claudia.Felser@cpfs.mpg.de

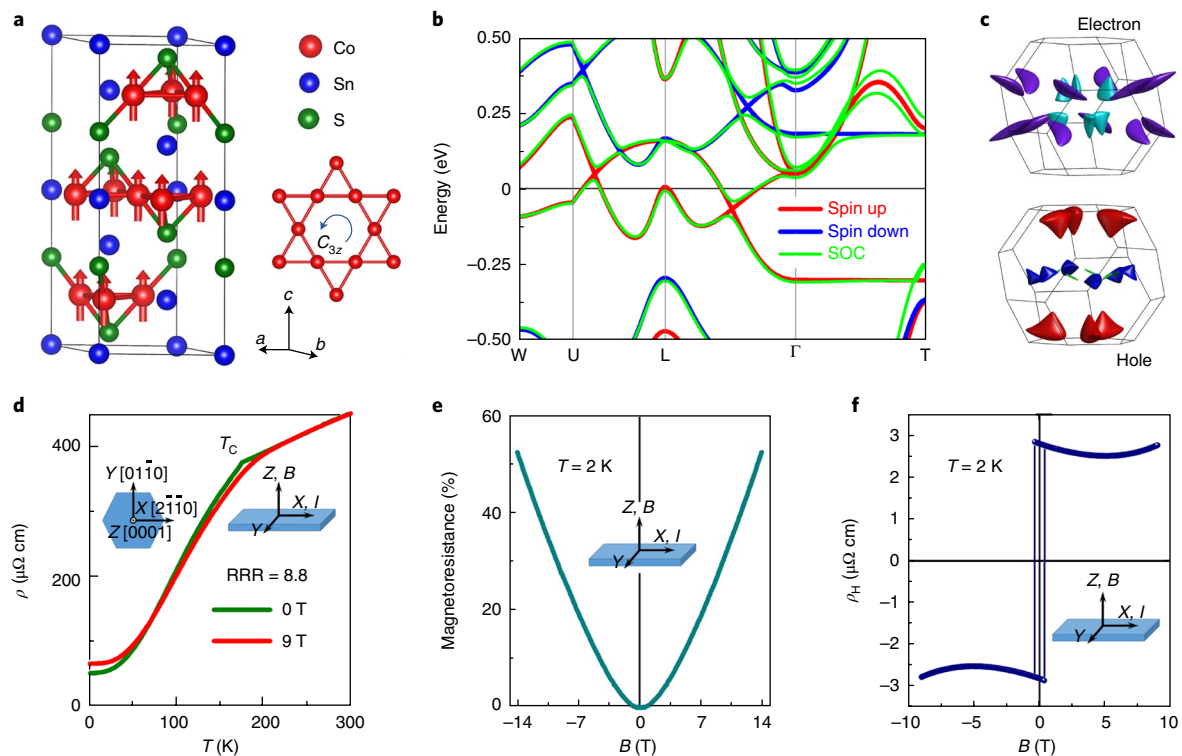


Fig. 1 | Crystal and electronic structures of $\text{Co}_3\text{Sn}_2\text{S}_2$ and the measured electric resistivity. **a**, Unit cell in a hexagonal setting. The cobalt atoms form a ferromagnetic kagome lattice with a C_{3z} -rotation. The magnetic moments are shown along the c axis. **b**, Energy dispersion of electronic bands along high-symmetry paths without and with spin-orbit coupling, respectively. ‘SOC’ denotes ‘spin-orbit coupling’. **c**, Fermi surfaces of two bands (upper: electron; lower: hole) under spin-orbit coupling calculations. Different colours indicate different parts of the Fermi surface in the Brillouin zone. **d**, Temperature dependences of the longitudinal electric resistivity (ρ) in zero-field and in a field of 9 T. In zero field, a residual resistivity ratio (RRR, $\rho_{300\text{K}}/\rho_{2\text{K}}$) value of 8.8 and a residual resistivity of $\rho_{2\text{K}} \sim 50 \mu\Omega \text{ cm}$ is observed; $\rho_{300\text{K}}$ and $\rho_{2\text{K}}$ are resistivities at 300 K and 2 K, respectively. **e**, Magnetoresistance measured in fields up to 14 T at 2 K, showing a non-saturated positive magnetoresistance. **f**, Hall data with a nonlinear behaviour at high fields, indicating the coexistence of electron and hole carriers at 2 K. All transport measurements depicted here were performed in an out-of-plane configuration with $I \parallel x \parallel [2\bar{1}\bar{1}0]$ and $B \parallel z \parallel [0001]$. The x and z axes, respectively, are thus parallel to the a and c axes shown in **a**. The hexagon in the inset to **d** shows the crystallographic orientations of the crystal. The insets to **d** (right inset), **e** and **f** show the directions of the current and magnetic field in the measurements.

in Fig. 1a, $\text{Co}_3\text{Sn}_2\text{S}_2$ crystallizes in a rhombohedral structure of the space group, $R\bar{3}m$ (no. 166)²⁷. The crystal possesses a quasi-2D Co_3Sn layer sandwiched between sulfur atoms, with the magnetic cobalt atoms arranged on a kagome lattice in the a - b plane in the hexagonal representation of the space group. Owing to the strong magnetic anisotropy, this material shows a long-range quasi-2D type of magnetism³⁰. Our magnetization measurements revealed a fairly low saturation field (~ 0.05 T) along the c axis and an extremely high saturation field (> 9 T) in the a - b plane, confirming a dominantly out-of-plane magnetization in $\text{Co}_3\text{Sn}_2\text{S}_2$ (see Supplementary Information). By itself, the dimensional restriction of the out-of-plane magnetization may be responsible for some of the interesting electronic and magnetic properties of this compound. We discuss band structure calculations of $\text{Co}_3\text{Sn}_2\text{S}_2$ with spin polarization along the c axis. The calculated magnetic moments without and with spin-orbit coupling are 0.33 and $0.30 \mu_{\text{B}}/\text{Co}$, respectively, which are very close to the experimental values of $0.29 \mu_{\text{B}}/\text{Co}$ obtained from neutron diffraction²⁹, $0.31 \mu_{\text{B}}/\text{Co}$ from magnetization measurements³⁰, and $0.30 \mu_{\text{B}}/\text{Co}$ from our measurement (see Supplementary Information). As expected, the calculation including spin-orbit coupling yields a more accurate result.

The band structures of $\text{Co}_3\text{Sn}_2\text{S}_2$ calculated without and with spin-orbit coupling are shown in Fig. 1b. The bands corresponding to the spin-down channel are insulating in character, with a gap of 0.35 eV, whereas the spin-up channel crosses the Fermi level and thus has metallic character. This half-metallic behaviour is

consistent with the results of previous studies on this compound^{30–32}. Furthermore, for the spin-up states, we observe linear band crossings along the Γ -L and L-U paths, just slightly above and below the Fermi energy, respectively. For finite spin-orbit coupling, these linear crossings open small gaps with band anti-crossings, and make this compound semimetal-like. The relatively small Fermi surfaces (Fig. 1c), showing the coexistence of holes and electrons, further corroborate the semi-metallic character of this compound. This calculated band structure is in good agreement with our angle-resolved photoemission spectroscopy (ARPES) measurements (see Supplementary Information). When these results are considered in conjunction with the ferromagnetism of $\text{Co}_3\text{Sn}_2\text{S}_2$ (refs 27–30), they suggest that a time-reversal-symmetry-breaking Weyl semimetal phase might be hidden in this compound.

In order to confirm this prediction, single crystals of $\text{Co}_3\text{Sn}_2\text{S}_2$ were grown for further experimental investigations (see Methods and Supplementary Information). The high quality of the crystals was confirmed by structure refinement based on single-crystal X-ray diffraction and topographic images of the hexagonal lattice array obtained using scanning tunnelling microscopy (see Supplementary Information). As shown in Fig. 1d, the longitudinal electric resistivity (ρ) decreases with decreasing temperature, showing a kink at $T_{\text{C}} = 175$ K and a moderate residual resistivity of approximately $50 \mu\Omega \text{ cm}$ at 2 K. In a high field of 9 T, a negative magnetoresistance appears around the Curie temperature owing to the spin-dependent scattering in magnetic systems. At low temperatures, the magnetoresistance

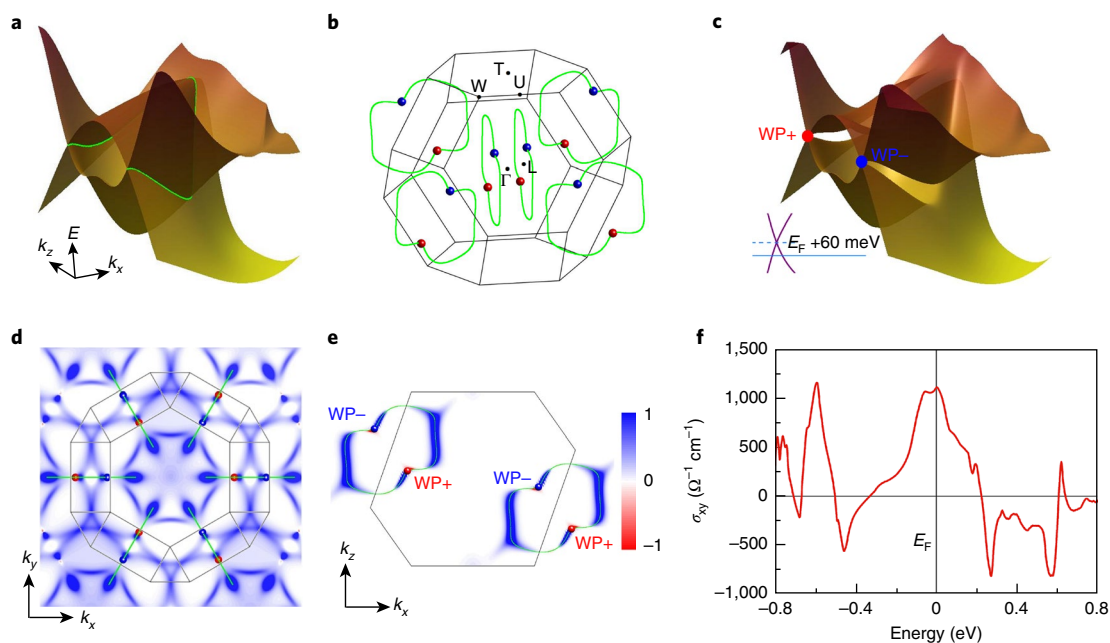


Fig. 2 | Theoretical calculations of the Berry curvature and anomalous Hall conductivity. **a**, Linear band crossings form a nodal ring in the mirror plane. **b**, Nodal rings and the distribution of the Weyl points in the Brillouin zone. **c**, Spin-orbit coupling breaks the nodal ring band structure into opened gaps and Weyl nodes. The Weyl nodes are located just 60 meV above the Fermi level, whereas the gapped nodal lines are distributed around the Fermi level. **d**, Berry curvature distribution projected to the k_x - k_y plane. **e**, Berry curvature distribution in the $k_y = 0$ plane. The colour bars for **d** and **e** are in arbitrary units. **f**, Energy dependence of the anomalous Hall conductivity in terms of the components of $\Omega_{yx}^z(\mathbf{k})$.

increases and becomes positive (Fig. 1d). This behaviour is further demonstrated by the field-dependent resistance (Fig. 1e). Importantly, the positive magnetoresistance shows no signature of saturation even up to 14 T, which is typical of a semimetal^{33,34}. The notable nonlinear field dependence of the Hall resistivity (ρ_{H1}) (Fig. 1f) further indicates the coexistence of hole and electron carriers at 2 K, which is in good agreement with our band structure calculations (Fig. 1b, c). By using the semiclassical two-band model³⁵, we extract the carrier densities of holes ($n_h \sim 9.3 \times 10^{19} \text{ cm}^{-3}$) and electrons ($n_e \sim 7.5 \times 10^{19} \text{ cm}^{-3}$) of our $\text{Co}_3\text{Sn}_2\text{S}_2$ samples. These relatively low carrier densities and a near compensation of charge carriers further confirm the semi-metallicity of $\text{Co}_3\text{Sn}_2\text{S}_2$.

In order to further analyse the topological character of $\text{Co}_3\text{Sn}_2\text{S}_2$ suggested by Fig. 1b, we now consider the linear band crossings in more detail. The space group $R\bar{3}m$ of $\text{Co}_3\text{Sn}_2\text{S}_2$ has one mirror plane (M_{010}). Without spin-orbit coupling, the interaction between spin-up and spin-down states is ignored and the mirror plane is a high-symmetry plane of the Hamiltonian. Thus, as they are protected by this mirror symmetry, the linear band crossing identified in Fig. 1b forms a nodal ring in the mirror plane based on the band inversion, as shown in Fig. 2a. Moreover, the linear crossings between the L- Γ and L-U paths are just single points on the ring. When the C_{32} -rotation and inversion symmetries of the material are considered, one finds a total of six nodal rings in the Brillouin zone, as shown schematically in Fig. 2b.

On taking spin-orbit coupling into account, the spin s_z is no longer a good quantum number and the mirror symmetry of the Hamiltonian is broken, which causes the linear crossings of the nodal lines to split, as presented in Fig. 2c. Interestingly, one pair of linear crossing points remains in the form of Weyl nodes along the former nodal line. These two Weyl nodes act as a monopole sink and source of Berry curvature (see Supplementary Information) and possess opposite topological charges of +1 and -1, respectively. In total, there are three such pairs of Weyl nodes in the first Brillouin zone due to the inversion and C_{32} -rotation symmetries of the crystal, and their distribution is presented in Fig. 2b. It is important

to emphasize that the Weyl nodes in $\text{Co}_3\text{Sn}_2\text{S}_2$ are only 60 meV above the charge neutrality point, which is much closer to the Fermi energy than for previously proposed magnetic Weyl semimetals. These Weyl nodes and non-trivial Weyl nodal rings together make this material exhibit a simple topological band structure around the Fermi level. It is thus easy to further observe the surface Fermi arcs³⁶. As a result, the Weyl-node-dominated physics in $\text{Co}_3\text{Sn}_2\text{S}_2$ should be prominent and easy to detect in experiments.

We now address the AHE response of $\text{Co}_3\text{Sn}_2\text{S}_2$ that can be expected from the particular band structure properties outlined above. In order to obtain a complete topological character, we integrated the Berry curvature $\Omega_{yx}^z(\mathbf{k})$ along k_z in the Brillouin zone. Our results reveal two main types of hot spot for the integrated Berry curvature: one located around the Weyl nodes, and the other located near the edge of the nodal lines (see Fig. 2d). To investigate the origin of the hot spot of the Berry curvature distribution, we choose the $k_y = 0$ plane, which includes two nodal rings and two pairs of Weyl nodes, as shown in Fig. 2e. We note that hot spots of the integrated Berry curvature are primarily determined by the shape of the nodal lines, and both types of hot spot observed here originate from the nodal-line-like band anti-crossing behaviour. Along the nodal ring, the component of the Berry curvature parallel to k_z leads to the larger hot spot we observe, whereas a different part around the Weyl node contributes to the smaller hot spot. Owing to the band anti-crossing behaviour and the position of the six Weyl nodal rings around the Fermi level, the calculated Berry curvature is clean and large, which should yield fascinating spin-electronic transport behaviours, including a large intrinsic AHE³.

The energy-dependent anomalous Hall conductivity (σ_{yx}) calculated from the Berry curvature is shown in Fig. 2f. As one can see from the figure, a large peak in σ_{yx} appears around E_p , with a maximum of $1,100 \Omega^{-1} \text{ cm}^{-1}$. Since σ_{yx} depends on the location of the Fermi level (see equation (3), Methods), it usually changes sharply as a function of energy. However, the peak in σ_{yx} in Fig. 2f stays above $1,000 \Omega^{-1} \text{ cm}^{-1}$ within an energy window of 100 meV below E_p . Therefore, we expect to observe a high σ_{yx} in experiments for charge

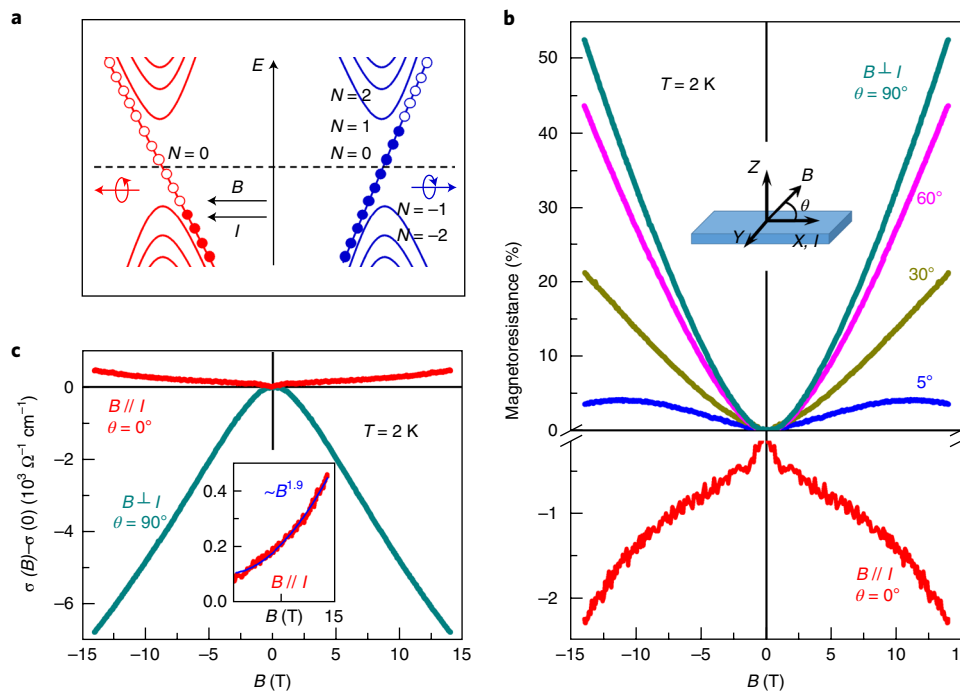


Fig. 3 | Chiral-anomaly-induced negative magnetoresistance. **a**, Schematic of the chiral anomaly. When the electron current I and magnetic field B are not perpendicular, charge carriers pump from one Weyl point to the other with opposite chirality, which leads to an additional contribution to the conductivity and a negative magnetoresistance. **b**, Angle dependence of magnetoresistance at 2 K. For $B \perp I // x // [2\bar{1}\bar{1}0]$ ($\theta = 90^\circ$), the magnetoresistance curve shows a positive, non-saturated behaviour up to 14 T. The magnetoresistance decreases rapidly with decreasing angle. A negative magnetoresistance appears when $B // I // x // [2\bar{1}\bar{1}0]$ ($\theta = 0^\circ$). A schematic diagram of the sample geometry is shown for the configuration. **c**, Magnetoconductance at 2 K in both cases of $B \perp I$ and $B // I$. The magnetoconductance is an equivalent description for the magnetoresistance. Positive magnetoconductance is observed in $\text{Co}_3\text{Sn}_2\text{S}_2$ when $B // I$. The fitting of the positive magnetoconductance in the inset shows an approximately $B^{1.9}$ dependence, which is very close to the parabolic ($\sim B^2$) field dependence for Weyl fermions.

neutral or slightly p -doped $\text{Co}_3\text{Sn}_2\text{S}_2$ samples. We also consider the non-collinear magnetic structure of the kagome lattice in $\text{Co}_3\text{Sn}_2\text{S}_2$. During spin tilting away from the c axis, the calculated σ_{yx} always stays above $1,000 \Omega^{-1} \text{cm}^{-1}$. The existence of Weyl nodes and the large anomalous Hall conductivity are robust against the change of the magnetic structure of $\text{Co}_3\text{Sn}_2\text{S}_2$ (see Supplementary Information).

A Weyl semimetal is expected to exhibit the so-called chiral anomaly³⁷ in transport, when the conservation of chiral charges is violated in the case of a parallel magnetic and electric field, as shown in Fig. 3a. We measured the impact of the magnetic field orientation on the transverse resistivity at 2 K (Fig. 3b). For $B \perp I$ ($\theta = 90^\circ$), a positive unsaturated magnetoresistance (also see Fig. 1e) is observed. The magnetoresistance decreases rapidly with decreasing θ . A clear negative magnetoresistance appears when $B // I$ ($\theta = 0^\circ$), which again does not saturate up to 14 T. As an equivalent description of the magnetoresistance, the magnetoconductance is shown in Fig. 3c. In the parallel case ($B // I$), the positive magnetoconductance can be described well by a near-parabolic field dependence³⁸, approximately as $B^{1.9}$, up to 14 T (inset of Fig. 3c). In this case, the charge carriers are pumped from one Weyl point to the other with opposite chirality, which leads to an additional contribution to the conductance, resulting in a negative magnetoresistance^{37,38}. The chiral anomaly evident from Fig. 3 represents an important signature of the Weyl fermions in $\text{Co}_3\text{Sn}_2\text{S}_2$.

Our transport measurements further verify the strong AHE induced by the Weyl band topology. An out-of-plane configuration of $I // x // [2\bar{1}\bar{1}0]$ and $B // z // [0001]$ was applied in these measurements (see Fig. 1d and Methods). As we observe in Fig. 4a, the anomalous Hall conductivity (σ_H^A) (see Methods) shows a high value of $1,130 \Omega^{-1} \text{cm}^{-1}$ at 2 K, which is in very good agreement with our predicted theoretical value (σ_{yx} , Fig. 2f). We also studied the

in-plane case ($I // x // [2\bar{1}\bar{1}0]$ and $B // y // [01\bar{1}0]$), for which the AHE disappears (not shown), due to strong magnetic and Berry-curvature anisotropies. Moreover, at temperatures below 100 K, for the out-of-plane case, $\sigma_H^A \sim 1,000 \Omega^{-1} \text{cm}^{-1}$ and is revealed to be independent of temperature (see also the inset of Fig. 4a, and note the logarithmic vertical axis). This robust behaviour against temperature indicates that the AHE is not governed by scattering events in the system. In addition, σ_H shows rectangular hysteresis loops with very sharp switching (Fig. 4b), and the coercive field is seen to increase with decreasing temperature, resulting in a value of 0.33 T at 2 K (also see Supplementary Information). As is evident from the figure, a large remanent Hall effect at zero field is observed in this material.

We plot ρ_H^A as a function of temperature in Fig. 4c. A large peak in ρ_H^A with a maximum of $44 \mu\Omega \text{cm}$ appears at 150 K. When σ_H^A is plotted against σ , as presented in Fig. 4d, we also find that σ_H^A is nearly independent of σ (that is, $\sigma_H^A \sim (\sigma)^0 = \text{constant}$) for temperatures below 100 K, as expected for an intrinsic AHE in the framework of the unified model for AHE physics^{39,40} (see Supplementary Information for more details). This independence of ρ_H^A with respect to both T and ρ indicates that the AHE originates only from the intrinsic scattering-independent mechanism, and is thus dominated by the Berry curvature in momentum space¹. This scaling behaviour is consistent with our first-principles calculations and provides another important signature for the magnetic Weyl fermions in $\text{Co}_3\text{Sn}_2\text{S}_2$.

In addition to a large σ_H^A , and arguably more importantly, the magnetic Weyl semimetal $\text{Co}_3\text{Sn}_2\text{S}_2$ also features a giant anomalous Hall angle that can be characterized by the ratio of σ_H^A/σ . The temperature dependence of σ_H^A/σ is shown in Fig. 5a. With increasing temperature, σ_H^A/σ first increases from 5.6% at 2 K, reaching a maximum

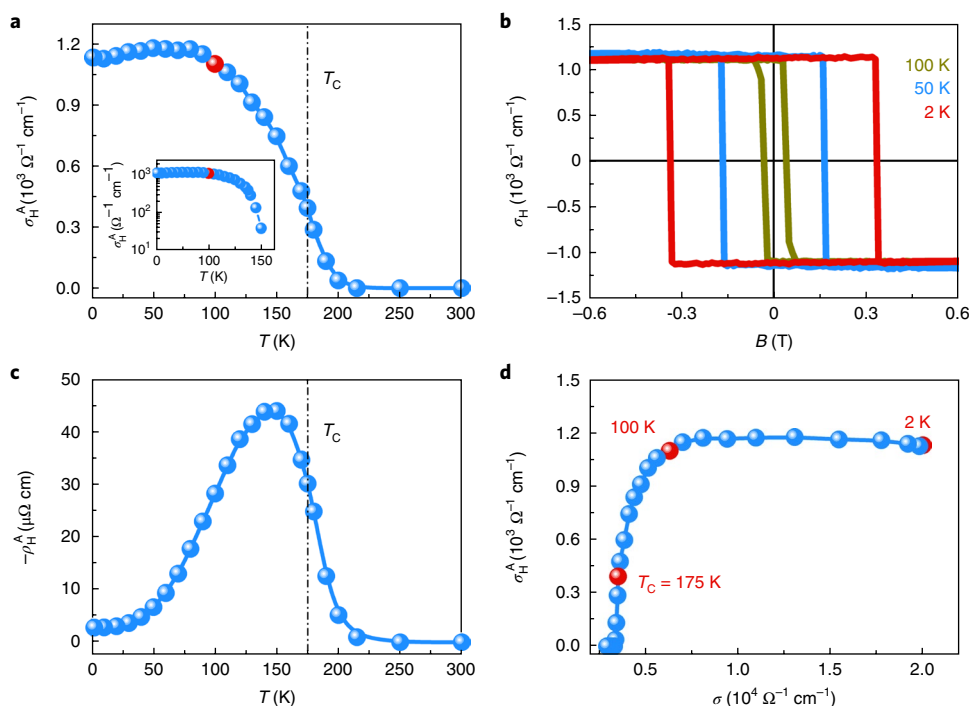


Fig. 4 | Transport measurements of the AHE. **a**, Temperature dependence of the anomalous Hall conductivity (σ_H^A) at zero magnetic field. The inset shows the logarithmic temperature dependence of σ_H^A . **b**, Field dependence of the Hall conductivity σ_H at 100, 50 and 2 K with $I // x // [2\bar{1}10]$ and $B // z // [0001]$. Hysteretic behaviour and sharp switching appears at temperatures below 100 K. **c**, Temperature dependence of the anomalous Hall resistivity (ρ_H^A). A peak appears around 150 K. Since ρ_H^A was derived by extrapolating the high-field part of ρ_H to zero field, non-zero values can be observed just above T_C due to the short-range magnetic exchange interactions enhanced by high fields. **d**, σ dependence of σ_H^A . The σ -independent σ_H^A (that is, $\sigma_H^A - (\sigma)^0 = \text{constant}$), below 100 K, puts this system into the intrinsic regime according to the unified model of AHE physics (for more details see Supplementary Information)^{39,40}.

of approximately 20% around 120 K, before decreasing again as the temperature increases above T_C . The contour plot of σ_H/σ with respect to B and T is depicted in Fig. 5b, and makes it intuitively clear that a giant Hall angle appears between 75 and 175 K irrespective of the magnetic fields magnitude. This can be straightforwardly understood by considering that σ_H^A arises from the Berry curvature of the occupied states. The band topology of these states is basically unaffected by the small energy scale of thermal excitations up to room temperature⁴¹. In other words, the topologically protected σ_H^A is relatively robust against temperature. In contrast, the Weyl-node-related charge conductivity (σ) is sensitive to temperature, due to electron–phonon scattering⁴². These behaviours are also shown in Fig. 5a. Therefore, σ_H^A/σ is expected to increase with increasing temperature in a wide temperature range below T_C . The semi-metallicity (low carrier density and low charge conductivity) largely improves the value of σ_H^A/σ in this system.

When compared to previously reported results for other AHE materials (see Fig. 5c), the value of the anomalous Hall angle in $\text{Co}_3\text{Sn}_2\text{S}_2$ observed in this work is seen to be the largest by a prominent margin. For most of these materials—formed mainly of ferromagnetic transition metals and alloys—the anomalous Hall conductivities originate from topologically trivial electronic bands. A typical feature of these materials is that both σ_H^A and σ are either large or small, and therefore σ_H^A/σ for these materials typically cannot be large. Although the magnetic-field-induced Weyl semimetal GdPtBi has a large σ_H^A/σ of 16%, its σ_H^A is very small and, moreover, it requires an external field to induce the Weyl phase²³. In contrast, owing to the non-trivial Berry curvature and the Weyl semi-metallic character, the kagome-lattice $\text{Co}_3\text{Sn}_2\text{S}_2$ possesses both a large σ_H^A and giant σ_H^A/σ , simultaneously and at zero magnetic field, which makes this system unusual among the known AHE materials.

As a consequence, a large anomalous Hall current can be expected in thin films of this material, which may even reach the limit of a quantized AHE with dissipationless quantum Hall edge states^{13,24,43,44}. In more general terms, a clean topological band structure induces both a large anomalous Hall conductivity and giant anomalous Hall angle (as demonstrated here for the Weyl semimetal $\text{Co}_3\text{Sn}_2\text{S}_2$), and so can be seen as a guide for the realization of strong AHE in (half-metallic) magnetic topological Weyl semimetals.

In summary, $\text{Co}_3\text{Sn}_2\text{S}_2$ is a Weyl semimetal candidate derived from a ferromagnetic kagome lattice. It is the first material that hosts both a large anomalous Hall conductivity and a giant anomalous Hall angle that originate from the Berry curvature. This compound is an ideal candidate for developing a quantum anomalous Hall state due to its long-range quasi-2D out-of-plane ferromagnetic order and simple electronic structure near the Fermi energy. Moreover, it is straightforward to grow large, high-quality, single crystals, which makes $\text{Co}_3\text{Sn}_2\text{S}_2$ and the Shandite family an excellent platform for comprehensive studies on topological electron behaviour. Our work motivates the study of the strong anomalous Hall effect based on magnetic Weyl semimetals, and establishes the ferromagnetic kagome-lattice Weyl semimetals as a key class of materials for fundamental research and applications connecting topological physics^{45–48} and spintronics^{49,50}.

Methods

Methods, including statements of data availability and any associated accession codes and references, are available at <https://doi.org/10.1038/s41567-018-0234-5>.

Received: 22 November 2017; Accepted: 28 June 2018;
Published online: 30 July 2018

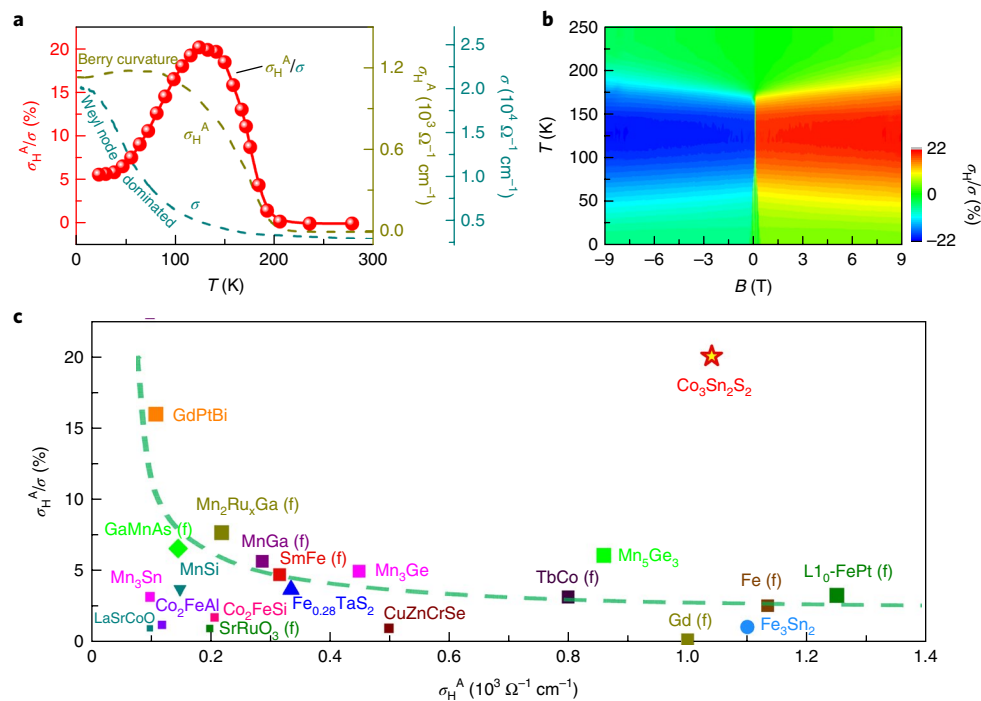


Fig. 5 | Transport measurements of the anomalous Hall angle. **a**, Temperature dependences of the anomalous Hall conductivity (σ_H^A), the charge conductivity (σ) and the anomalous Hall angle (σ_H^A/σ) at zero magnetic field. Since the ordinary Hall effect vanishes at zero field, the anomalous Hall contribution prevails (see Supplementary Information). **b**, Contour plots of the Hall angle in the B - T space. **c**, Comparison of our σ_H^A -dependent anomalous Hall angle results and previously reported data for other AHE materials. ‘(f)’ denotes thin-film materials. The dashed line is a guide to the eye. The reported data were taken from references that can be found in the Supplementary Information.

References

- Nagaosa, N., Sinova, J., Onoda, S., MacDonald, A. H. & Ong, N. P. Anomalous Hall effect. *Rev. Mod. Phys.* **82**, 1539–1592 (2010).
- Fang, Z. et al. The anomalous Hall effect and magnetic monopoles in momentum space. *Science* **302**, 92–95 (2003).
- Haldane, F. D. M. Berry curvature on the Fermi surface: Anomalous Hall effect as a topological Fermi-liquid property. *Phys. Rev. Lett.* **93**, 206602 (2004).
- Xiao, D., Chang, M. C. & Niu, Q. Berry phase effects on electronic properties. *Rev. Mod. Phys.* **82**, 1959–2007 (2010).
- Nakatsuji, S., Kiyohara, N. & Higo, T. Large anomalous Hall effect in a non-collinear antiferromagnet at room temperature. *Nature* **527**, 212–215 (2015).
- Weng, H. M., Fang, C., Fang, Z., Bernevig, B. A. & Dai, X. Weyl semimetal phase in noncentrosymmetric transition-metal monophosphides. *Phys. Rev. X* **5**, 011029 (2015).
- Yan, B. & Felser, C. Topological materials: Weyl semimetals. *Annu. Rev. Condens. Matter Phys.* **8**, 337–354 (2017).
- Weng, H. M., Yu, R., Hu, X., Dai, X. & Fang, Z. Quantum anomalous Hall effect and related topological electronic states. *Adv. Phys.* **64**, 227–282 (2015).
- Liu, C.-X., Zhang, S.-C. & Qi, X.-L. The quantum anomalous Hall effect: Theory and experiment. *Annu. Rev. Condens. Matter Phys.* **7**, 301–321 (2016).
- Yu, R. et al. Quantized anomalous Hall effect in magnetic topological insulators. *Science* **329**, 61–64 (2010).
- Chang, C.-Z. et al. Experimental observation of the quantum anomalous Hall effect in a magnetic topological insulator. *Science* **340**, 167–170 (2013).
- Fang, C., Gilbert, M. J. & Bernevig, B. A. Large-Chern-number quantum anomalous Hall effect in thin-film topological crystalline insulators. *Phys. Rev. Lett.* **112**, 046801 (2014).
- Kou, X. et al. Scale-invariant quantum anomalous Hall effect in magnetic topological insulators beyond the two-dimensional limit. *Phys. Rev. Lett.* **113**, 137201 (2014).
- Burkov, A. A. & Balents, L. Weyl semimetal in a topological insulator multilayer. *Phys. Rev. Lett.* **107**, 127205 (2011).
- Zyuzin, A. A., Wu, S. & Burkov, A. A. Weyl semimetal with broken time reversal and inversion symmetries. *Phys. Rev. B* **85**, 165110 (2012).
- Wang, X., Vanderbilt, D., Yates, J. R. & Souza, I. Fermi-surface calculation of the anomalous Hall conductivity. *Phys. Rev. B* **76**, 195109 (2007).
- Burkov, A. A. Anomalous Hall effect in Weyl metals. *Phys. Rev. Lett.* **113**, 187202 (2014).
- Wan, X. G., Turner, A. M., Vishwanath, A. & Savrasov, S. Y. Topological semimetal and Fermi-arc surface states in the electronic structure of pyrochlore iridates. *Phys. Rev. B* **83**, 205101 (2011).
- Xu, G., Weng, H. M., Wang, Z. J., Dai, X. & Fang, Z. Chern semimetal and the quantized anomalous Hall effect in HgCr_2Se_4 . *Phys. Rev. Lett.* **107**, 186806 (2011).
- Kübler, J. & Felser, C. Weyl points in the ferromagnetic Heusler compound Co_2MnAl . *Europhys. Lett.* **114**, 47005 (2016).
- Wang, Z. J. et al. Time-reversal-breaking Weyl fermions in magnetic Heusler alloys. *Phys. Rev. Lett.* **117**, 236401 (2016).
- Chang, G. Q. et al. Room-temperature magnetic topological Weyl fermion and nodal line semimetal states in half-metallic Heusler Co_2TiX ($X = \text{Si, Ge, or Sn}$). *Sci. Rep.* **6**, 38839 (2016).
- Suzuki, T. et al. Large anomalous Hall effect in a half-Heusler antiferromagnet. *Nat. Phys.* **12**, 1119–1123 (2016).
- Ohgushi, K., Murakami, S. & Nagaosa, N. Spin anisotropy and quantum Hall effect in the kagome lattice: Chiral spin state based on a ferromagnet. *Phys. Rev. B* **62**, R6065–R6068 (2000).
- Xu, G., Lian, B. & Zhang, S.-C. Intrinsic quantum anomalous Hall effect in the Kagome lattice $\text{Cs}_2\text{LiMn}_3\text{F}_{12}$. *Phys. Rev. Lett.* **115**, 186802 (2015).
- Ye, L. et al. Massive Dirac fermions in a ferromagnetic kagome metal. *Nature* **555**, 638–642 (2018).
- Wehrich, R., Anusca, I. & Zabel, M. Half-antiperovskites: Structure and type-antitype relations of Shandites $\text{M}_{3/2}\text{AS}$ ($M = \text{Co, Ni; A = In, Sn}$). *Z. Anorg. Allg. Chem.* **631**, 1463–1470 (2005).
- Wehrich, R. & Anusca, I. Half antiperovskites. III - Crystallographic and electronic structure effects in $\text{Sn}_{2-x}\text{In}_x\text{Co}_3\text{S}_2$. *Z. Anorg. Allg. Chem.* **632**, 1531–1537 (2006).
- Vaqueiro, P. & Sobany, G. G. A powder neutron diffraction study of the metallic ferromagnet $\text{Co}_3\text{Sn}_2\text{S}_2$. *Solid State Sci.* **11**, 513–518 (2009).
- Schnelle, W. et al. Ferromagnetic ordering and half-metallic state of $\text{Sn}_2\text{Co}_3\text{S}_2$ with the Shandite-type structure. *Phys. Rev. B* **88**, 144404 (2013).
- Dedkov, Y. S., Holder, M., Molodtsov, S. L. & Rosner, H. Electronic structure of shandite $\text{Co}_3\text{Sn}_2\text{S}_2$. *J. Phys. Conf. Ser.* **100**, 072011 (2008).
- Holder, M. et al. Photoemission study of electronic structure of the half-metallic ferromagnet $\text{Co}_3\text{Sn}_2\text{S}_2$. *Phys. Rev. B* **79**, 205116 (2009).
- Ali, M. N. et al. Large, non-saturating magnetoresistance in WTe_2 . *Nature* **514**, 205–208 (2014).

34. Kumar, N. et al. Extremely high magnetoresistance and conductivity in the type-II Weyl semimetals WP_2 and MoP_2 . *Nat. Commun.* **8**, 1642 (2017).
35. Ziman, J. M. *Electrons and Phonons: Theory of Transport Phenomena in Solids* (Oxford Univ. Press, Oxford, 1960).
36. Xu, Q. et al. Topological surface Fermi arcs in the magnetic Weyl semimetal $Co_3Sn_2S_2$. *Phys. Rev. B* **97**, 235416 (2018).
37. Nielsen, H. B. & Ninomiya, M. The Adler–Bell–Jackiw anomaly and Weyl fermions in a crystal. *Phys. Lett. B* **130**, 389–396 (1983).
38. Son, D. T. & Spivak, B. Z. Chiral anomaly and classical negative magnetoresistance of Weyl metals. *Phys. Rev. B* **88**, 104412 (2013).
39. Onoda, S., Sugimoto, N. & Nagaosa, N. Intrinsic versus extrinsic anomalous Hall effect in ferromagnets. *Phys. Rev. Lett.* **97**, 126602 (2006).
40. Miyasato, T. et al. Crossover behavior of the anomalous Hall effect and anomalous Nernst effect in itinerant ferromagnets. *Phys. Rev. Lett.* **99**, 086602 (2007).
41. Yue, D. & Jin, X. Towards a better understanding of the anomalous Hall effect. *J. Phys. Soc. Jpn* **86**, 011006 (2016).
42. Gantmakher, V. F. The experimental study of electron–phonon scattering in metals. *Rep. Prog. Phys.* **37**, 317–362 (1974).
43. Checkelsky, J. G. et al. Trajectory of the anomalous Hall effect towards the quantized state in a ferromagnetic topological insulator. *Nat. Phys.* **10**, 731–736 (2014).
44. Samarth, N. Quantum materials discovery from a synthesis perspective. *Nat. Mater.* **16**, 1068–1076 (2017).
45. Chan, C.-K., Lee, P. A., Burch, K. S., Han, J. H. & Ran, Y. When chiral photons meet chiral fermions: Photoinduced anomalous Hall effects in Weyl semimetals. *Phys. Rev. Lett.* **116**, 026805 (2016).
46. Ikhlas, M. et al. Large anomalous Nernst effect at room temperature in a chiral antiferromagnet. *Nat. Phys.* **13**, 1085–1090 (2017).
47. Rajamathi, C. R. et al. Weyl semimetals as hydrogen evolution catalysts. *Adv. Mater.* **29**, 1606202 (2017).
48. Yang, B.-J., Moon, E.-G., Isobe, H., & Nagaosa, N. Quantum criticality of topological phase transitions in three-dimensional interacting electronic systems. *Nat. Phys.* **10**, 774–778 (2014).
49. Kurebayashi, D. & Nomura, K. Voltage-driven magnetization switching and spin pumping in Weyl semimetals. *Phys. Rev. Appl.* **6**, 044013 (2016).
50. Tokura, Y., Kawasaki, M. & Nagaosa, N. Emergent functions of quantum materials. *Nat. Phys.* **13**, 1056–1068 (2017).

Acknowledgements

This work was financially supported by the European Research Council (ERC) Advanced Grant (No. 291472) 'IDEA Heusler!' and ERC Advanced Grant (No. 742068) 'TOPMAT'. E.L. acknowledges support from the Alexander von Humboldt Foundation of Germany for his Fellowship and from the National Natural Science Foundation of China for his Excellent Young Scholarship (No. 51722106).

Author contributions

The project was conceived by E.L. and C.F. Single crystals were grown by E.L., who performed the structural, magnetic and transport measurements with assistance from A.S., J.K., S.Y., V.S., H.B., N.K. and W.S. The STM characterizations were performed by L.J. and S.W. The ARPES measurements were conducted by D.L., A.L. and Y.C. The static high-magnetic-field measurements were performed and analysed by Z.W., C.X., N.K., C.S. and L.J. The theoretical calculations were carried out by Y.S., L.M., Q.X. and E.L. All the authors discussed the results. The paper was written by E.L., Y.S. and S.T.B.G. with feedback from all the authors. The project was supervised by C.F.

Competing interests

The authors declare no competing interests.

Additional information

Supplementary information is available for this paper at <https://doi.org/10.1038/s41567-018-0234-5>.

Reprints and permissions information is available at www.nature.com/reprints.

Correspondence and requests for materials should be addressed to E.L. or Y.S. or C.F.

Publisher's note: Springer Nature remains neutral with regard to jurisdictional claims in published maps and institutional affiliations.

Methods

Single-crystal growth. The single crystals of $\text{Co}_3\text{Sn}_2\text{S}_2$ were grown by self-flux methods with Sn as flux or with the congruent composition in a graphite crucible sealed in a quartz tube (see Supplementary Information). The stoichiometric samples (Co:Sn:S = 3:2:2) were heated to 1,000 °C over 48 hours and kept there for 24 hours before being slowly cooled to 600 °C over seven days. The samples were kept at 600 °C for 24 hours to obtain homogeneous and ordered crystals. The compositions of crystals were checked by energy-dispersive X-ray spectroscopy. The crystals were characterized by powder X-ray diffraction as single phase with a Shandite-type structure. The lattice parameters at room temperature are $a = 5.3689 \text{ \AA}$ and $c = 13.176 \text{ \AA}$. The single crystals and orientations were confirmed by a single-crystal X-ray diffraction technique.

Scanning tunnelling microscopy (STM). Topographic images of the crystal surface were characterized by cryogenic STM, taken at conditions of $T = 2.5 \text{ K}$, a bias voltage of $V_b = 100 \text{ mV}$ and a tunnel current of $I_t = 500 \text{ pA}$. The sample was cleaved in situ ($p \leq 2 \times 10^{-9} \text{ Pa}$) at 20 K. The high quality of the single crystals was confirmed by STM (see Supplementary Information).

Magnetization measurements. Magnetization measurements were carried out on oriented crystals with the magnetic field applied along both the a and c axes using a vibrating sample magnetometer (MPMS 3, Quantum Design). The results show an extremely strong magnetic anisotropy in $\text{Co}_3\text{Sn}_2\text{S}_2$ (see Supplementary Information).

Out-of-plane transport measurements. The out-of-plane transport measurements on longitudinal charge and Hall resistivities, with $B \parallel z \parallel [0001]$ and $I \parallel x \parallel [2\bar{1}\bar{1}0]$, were performed on a PPMS 9 (Quantum Design) using the low-frequency alternating current (ACT) option. The standard four-probe method was used to measure the longitudinal electrical resistivity, whereas for the Hall resistivity measurements, the five-probe method was used with a balance protection meter to eliminate possible magnetoresistance signals. The charge and Hall resistivities were measured in turn at each temperature.

Angle-dependent longitudinal electric resistivity. The angle dependence of longitudinal electric resistivity was measured on a PPMS DynaCool (Quantum Design) using the 'DC Resistivity' option. For the angle-dependent measurements, $B \parallel \theta$ and $I \parallel x \parallel [2\bar{1}\bar{1}0]$, while θ is the angle with respect to $x \parallel [2\bar{1}\bar{1}0]$. The currents were always applied along the a axis, for example, $I \parallel x \parallel [2\bar{1}\bar{1}0]$ (a axis = x axis). Different crystals, grown by two self-flux methods and with different RRR ($\rho_{300\text{K}}/\rho_{2\text{K}}$) values, were used in this study.

Analysis of Hall effect and semi-metallicity. At high temperatures ($50 \text{ K} < T < T_C$), the Hall signal shows a linear field-dependent behaviour after saturation. At low temperatures ($T < 50 \text{ K}$), a notable nonlinear field dependence of the Hall resistivity is observed, indicating the existence of two types of carriers (electrons and holes). The electron carriers appear at low temperatures. The single-band and two-band models were thus applied to extract the pure anomalous Hall resistivity, carrier densities and mobilities, for high-temperature and low-temperature cases, respectively.

The anomalous Hall conductivity was calculated by

$$\sigma_{\text{H}}^{\text{A}} = -\frac{\rho_{\text{H}}^{\text{A}}}{(\rho_{\text{H}}^{\text{A}})^2 + \rho^2} \quad (1)$$

Here $\rho_{\text{H}}^{\text{A}}$ is the anomalous Hall resistivity at zero field and ρ is the longitudinal resistivity at zero field.

The two-band model³⁵ was applied to extract the densities of both carriers at low temperatures.

$$\begin{aligned} \sigma(B) &= \frac{n_{\text{h}} e \mu_{\text{h}}}{1 + \mu_{\text{h}}^2 B^2} + \frac{n_{\text{e}} e \mu_{\text{e}}}{1 + \mu_{\text{e}}^2 B^2} \\ \sigma_{\text{H}}(B) &= \frac{n_{\text{h}} e \mu_{\text{h}}^2 B}{1 + \mu_{\text{h}}^2 B^2} + \frac{n_{\text{e}} e \mu_{\text{e}}^2 B}{1 + \mu_{\text{e}}^2 B^2} \end{aligned} \quad (2)$$

Here B is the applied magnetic field, $\sigma(B)$ is the longitudinal charge conductivity, $\sigma_{\text{H}}(B)$ is the anomalous Hall effect, n_{h} is the carrier concentration of holes, μ_{h} is the carrier mobility of holes, n_{e} is the carrier concentration of electrons and μ_{e} is the carrier mobility of electrons.

Longitudinal magnetoresistance in static high magnetic fields. The field-dependent longitudinal magnetoresistance was measured in static magnetic fields as high as 37 T, by a standard four-probe method in a ^3He cryostat with $B \parallel c$ axis, using a hybrid magnet at the High Magnetic Field Laboratory, Chinese Academy of Sciences. The current was 5 mA, modulated at a frequency of 13.7 Hz by means of a Keithley 6221. The voltage was measured by a SR830 Lock-In Amplifier. The Shubnikov–de Haas (SdH) quantum oscillations of magnetoresistivity were observed above 17 T in the present crystal. A cubic polynomial background was subtracted from the resistivity data. For the fast Fourier transform, a Hanning window was applied in the Origin software.

Density functional theory (DFT) calculations. The electronic structure calculations were performed on the basis of DFT using the Vienna ab-initio simulation package (VASP)⁵¹. The exchange and correlation energies were considered in the generalized gradient approximation (GGA), following the Perdew–Burke–Ernzerhof parametrization scheme⁵². We have projected the Bloch wavefunctions into Wannier functions⁵³, and constructed the tight-binding model Hamiltonian based on Wannier functions. The anomalous Hall conductivity and Berry curvature were calculated by the Kubo formula approach in the linear response and clean limit⁴:

$$\begin{aligned} \sigma_{yx}^z(E_F) &= e^2 \hbar \left(\frac{1}{2\pi} \right)^3 \int_{\mathbf{k}} d\mathbf{k} \sum_{E(n,\mathbf{k}) < E_F} f(n,\mathbf{k}) \Omega_{n,yx}^z(\mathbf{k}) \\ \Omega_{n,yx}^z(\mathbf{k}) &= \\ \text{Im} \sum_{n' \neq n} \frac{\langle u(n,\mathbf{k}) | \hat{v}_y | u(n',\mathbf{k}) \rangle \langle u(n',\mathbf{k}) | \hat{v}_x | u(n,\mathbf{k}) \rangle - (x \leftrightarrow y)}{(E(n,\mathbf{k}) - E(n',\mathbf{k}))^2} \end{aligned} \quad (3)$$

where $f(n,\mathbf{k})$ is the Fermi–Dirac distribution, $E(n,\mathbf{k})$ is the eigenvalue of the n th eigenstate of $|u(n,\mathbf{k})\rangle$ at the \mathbf{k} point, and $\hat{v}_{x(y)} = \frac{1}{\hbar} \frac{\partial H(\mathbf{k})}{\partial k_{x(y)}}$ is the velocity operator.

The numerical integration was performed using a $501 \times 501 \times 501$ k -grid. The Fermi surfaces were calculated by means of a k -grid of $120 \times 120 \times 120$ from the tight-binding model Hamiltonian, and the frequencies of electron oscillations were calculated from the extremal cross-sectional areas of the Fermi surface perpendicular to the applied magnetic field (see Supplementary Information).

Angle-resolved photoemission spectroscopy (ARPES). ARPES measurements on single crystals were performed at beamline BL5-2 of the Stanford Synchrotron Radiation Lightsource, SLAC National Accelerator Laboratory, and beamline BL10.0.1 of the Advanced Light Source (ALS). The data were recorded by a Scienta R4000 Analyzer at $p = 4 \times 10^{-9} \text{ Pa}$ at 20 K in both facilities. The total convolved energy and angle resolutions were $E = 10$ to 20 meV and $\theta = 0.2^\circ$, respectively. Good agreements of the Fermi surfaces and energy dispersions from ARPES measurements and DFT calculations are also obtained (see Supplementary Information).

Data availability. The data that support the plots within this paper and other findings of this study are available from the corresponding author upon reasonable request.

References

- Kresse, G. & Furthmüller, J. Efficient iterative schemes for *ab initio* total-energy calculations using a plane-wave basis set. *Phys. Rev. B* **54**, 11169–11186 (1996).
- Perdew, J. P., Burke, K. & Ernzerhof, M. Generalized gradient approximation made simple. *Phys. Rev. Lett.* **77**, 3865–3868 (1996).
- Mostofi, A. A. et al. wannier90: A tool for obtaining maximally-localised Wannier functions. *Comput. Phys. Commun.* **178**, 685–699 (2008).